

astrophysical simulations (Fig. 3A; see methods), performed with mass-ejection rates (22) and magnetic field strengths (10) typical of YSOs. We further verified that the range of density and temperature conditions found along the jet implies that the material within covers the full range of ionization fraction, with most of the jet part being only weakly ionized, consistent with observations (23). We see the principal dynamics and features of the laboratory flows also in the simulation results, which support the scalability of the laboratory experiment. We varied the wind and field parameters extensively with detailed numerical simulations to verify that the poloidal-field-induced jet collimation mechanism was a very robust process.

An interesting outcome of our study is that typical YSOs should then have a stationary region of shock-heated plasma that forms within a few tens to 100 AU from the wind source (see Fig. 3A). This numerical prediction can be directly compared to the analysis of observations made over more than one decade using x-ray satellites that have revealed (see Fig. 3C) bright sources of stationary x-ray emission zones located at the base of jets (~100 AU from the source) emerging from a YSO (24–26) and distinct from it. They have not been explained so far by self-collimation models of jet formation but are still consistent with the process revealed here (Fig. 3B).

We have therefore proposed a simple and plausible scenario for the collimation of a narrow stable jet past its launching phase (1, 2) that is consistent with recent astrophysical observations (10, 24, 25). In addition to helping to advance the understanding of jet–core interaction in YSOs, our work enables studying and/or modeling important aspects of jet physics in the laboratory. These include, e.g., transverse instabilities that can affect the jet structure, or episodic ejections, i.e., multicomponent and time-dependent interacting winds, which can be easily simulated in the laboratory by using multiple laser pulses separated by a few nanoseconds. Producing such magnetized narrow plasma columns and letting them strike a solid will also uniquely allow the study of plasma dynamics in accretion columns in young stars; that is, one can model magnetic arches that are loaded with disk material that free-falls toward the star. Beyond these aspects, adapting the present experimental work to other configurations will permit advances in resolving pending questions about a wide range of astrophysical and plasma physics systems where magnetic fields are thought to play an important role.

REFERENCES AND NOTES

1. A. Frank, T. P. Ray, S. Cabrit, P. Hartigan, H. G. Arce, F. Bacciotti, J. Bally, M. Benisty, J. Eisloffel, M. Güdel, S. Lebedev, B. Nisini, A. Raga, *Jets and Outflows From Star to Cloud: Observations Confront Theory, in Protostars and Planets VI*, H. Beuther, R. Klessen, C. Dullemond, Th. Henning, Eds. (Univ. of Arizona Press, Tucson, 2014).
2. R. D. Blandford, D. G. Payne, *Mon. Not. R. Astron. Soc.* **199**, 883–903 (1982).
3. J. Ferreira, *Astron. Astrophys.* **319**, 340–359 (1997).
4. R. E. Ainsworth, T. P. Ray, A. M. M. Scaife, J. S. Greaves, R. J. Beswick, *Mon. Not. R. Astron. Soc.* **436**, L64–L68 (2013).
5. M. Stute, J. Gracia, K. Tsinganos, N. Vlahakis, *Astron. Astrophys.* **516**, A6 (2010).
6. R. Moll, H. C. Spruit, M. Obergaulinger, *Astron. Astrophys.* **492**, 621–630 (2008).
7. T. Matsakos et al., *Astron. Astrophys.* **502**, 217–229 (2009).
8. H. C. Spruit, T. Foglizzo, R. Stehle, *Mon. Not. R. Astron. Soc.* **288**, 333–342 (1997).
9. S. Matt, R. Winglee, K.-H. Böhm, *Mon. Not. R. Astron. Soc.* **345**, 660–670 (2003).
10. P. Hartigan, A. Frank, P. Varnière, E. G. Blackman, *Astrophys. J.* **661**, 910–918 (2007).
11. N. L. Chapman et al., *Astrophys. J.* **770**, 151 (2013).
12. A. Ciardi et al., *Phys. Rev. Lett.* **110**, 025002 (2013).
13. F. Favata et al., *Astron. Astrophys.* **450**, L17–L20 (2006).
14. J. A. Stamper, *Laser Part. Beams* **9**, 841–862 (1991).
15. B. Albertazzi et al., *Rev. Sci. Instrum.* **84**, 043505 (2013).
16. D. D. Ryutov, R. P. Drake, B. A. Remington, *Astrophys. J. Suppl. Ser.* **127**, 465–468 (2000).
17. D. Farley et al., *Phys. Rev. Lett.* **83**, 1982–1985 (1999).
18. B. Loupias et al., *Phys. Rev. Lett.* **99**, 265001 (2007).
19. Ph. Nicolai et al., *Phys. Plasmas* **15**, 082701 (2008).
20. A. Faenov et al., *Phys. Scr.* **53**, 591–596 (1996).
21. B. Balick, A. Frank, *Annu. Rev. Astron. Astrophys.* **40**, 439–486 (2002).
22. S. Cabrit, in *Star-Disk Interaction in Young Stars*, Proceedings IAU Symp. no. 243, J. Bouvier, I. Appenzeller, Eds. (Cambridge Univ. Press, Cambridge, 2007), pp. 203–214.
23. L. Mauri et al., *Astron. Astrophys.* **565**, A110 (2014).
24. M. Güdel, S. L. Skinner, M. Audard, K. R. Briggs, S. Cabrit, *Astron. Astrophys.* **478**, 797–807 (2008).
25. P. C. Schneider, H. M. Günther, J. H. M. M. Schmitt, *Astron. Astrophys.* **530**, A123 (2011).
26. R. Bonito et al., *Astrophys. J.* **737**, 54 (2011).

ACKNOWLEDGMENTS

We acknowledge the support of the LULI teams and of S. Dittrich and S. Nitsche (Helmholtz-Zentrum Dresden-Rossendorf) and discussions with P. Audebert. This work was supported by grant EL127 from Région Ile-de-France, Agence Nationale de la recherche (ANR) white grant 12-BS09-025-01 SILAMPA, grant ELAM from Réseau thématique de recherche avancé (RTRA)-Saclay, a grant from RTRA-Triangle de la Physique, grants Engineering and Physical Sciences Research Council (EPSRC) EP/1029206/1 and EP/J500094/1, and the Natural Sciences and Engineering Research Council of Canada (NSERC) Discovery grant 26558-2007 RGPIN. This work was partly done within the LABEX Plas@Par project and received financial state aid managed by the Agence Nationale de la Recherche, as part of the program “Investissements d’avenir” under the reference ANR-11-IDEX-0004-02. This work was supported in part by the Ministry of Education and Science of the Russian Federation under contract no. 14.Z50.31.0007. S.N.C. acknowledges the support received during this work by NSF grant 1064468. Experimental data and simulations are, respectively, archived on servers at LULI and LERMA laboratories and can be consulted upon demand. Part of the experimental system is covered by a patent (1000183285, 2013, Institut National de la Propriété Industrielle–France).

SUPPLEMENTARY MATERIALS

www.sciencemag.org/content/346/6207/325/suppl/DC1
Materials and Methods
References (27–32)

6 August 2014; accepted 17 September 2014
10.1126/science.1259694

OPTICS

Loss-induced suppression and revival of lasing

B. Peng,^{1*} Ş. K. Özdemir,^{1*†} S. Rotter,² H. Yilmaz,¹ M. Liertzer,² F. Monifi,¹ C. M. Bender,³ F. Nori,^{4,5} L. Yang^{1†}

Controlling and reversing the effects of loss are major challenges in optical systems.

For lasers, losses need to be overcome by a sufficient amount of gain to reach the lasing threshold. In this work, we show how to turn losses into gain by steering the parameters of a system to the vicinity of an exceptional point (EP), which occurs when the eigenvalues and the corresponding eigenstates of a system coalesce. In our system of coupled microresonators, EPs are manifested as the loss-induced suppression and revival of lasing. Below a critical value, adding loss annihilates an existing Raman laser. Beyond this critical threshold, lasing recovers despite the increasing loss, in stark contrast to what would be expected from conventional laser theory. Our results exemplify the counterintuitive features of EPs and present an innovative method for reversing the effect of loss.

Dissipation is ubiquitous in nature; the states of essentially all physical systems thus have a finite decay time. A proper description of this situation requires a departure from conventional Hermitian models with real eigenvalues and orthogonal eigenstates

to non-Hermitian models featuring complex eigenvalues and nonorthogonal eigenstates (1–3). When tuning the parameters of such a dissipative system, its complex eigenvalues and the corresponding eigenstates may coalesce, giving rise to a non-Hermitian degeneracy, also called an exceptional point (EP) (4). The presence of such an EP has a dramatic effect on the system, leading to nontrivial physics with interesting counterintuitive features such as resonance trapping (5), a mode exchange when encircling an EP (6), and a singular topology in the parameter landscape (7). These characteristics can control the flow of light in optical devices with both loss and gain. In particular, waveguides with parity-time symmetry (8), where loss and gain are balanced, have attracted enormous attention (9, 10), with effects

¹Department of Electrical and Systems Engineering, Washington University, St. Louis, MO 63130, USA. ²Institute for Theoretical Physics, Vienna University of Technology, A-1040 Vienna, Austria. ³Department of Physics, Washington University, St. Louis, MO 63130, USA. ⁴Center for Emergent Matter Science, RIKEN, Wako-shi, Saitama 351-0198, Japan. ⁵Department of Physics, University of Michigan, Ann Arbor, MI 48109, USA.

*These authors contributed equally to this work. †Corresponding author. E-mail: ozdemir@ese.wustl.edu (S.K.O.); yang@ese.wustl.edu (L.Y.)

such as loss-induced transparency (11), unidirectional invisibility (12), and reflectionless scattering (13, 14) having already been observed.

Theoretical work indicates that EPs give rise to many more intriguing effects when they occur near the lasing regime; for example, enhancement of the laser linewidth (15, 16), fast self-pulsations (15), and a pump-induced lasing death (17). Realizing such anomalous phenomena, however, requires moving from waveguides to resonators, which can trap and amplify light resonantly beyond the lasing threshold. With the availability of such devices (18, 19), we discuss here the most counterintuitive aspect, namely, that close to an exceptional point, lasing should be inducible solely by adding loss to a resonator.

Our experimental system (20) consists of two directly coupled silica whispering-gallery-mode resonators (WGMRs), μR_1 and μR_2 , each coupled to a different fiber-taper, WG1 and WG2 (Fig. 1A and supplementary text S1). The resonance frequencies of the WGMRs were tuned to be the same via the thermo-optic effect, and a controllable coupling strength κ was achieved between the WGMRs by adjusting the interresonator distance. To observe its behavior in the vicinity of an EP, the system was steered parametrically via κ and an additional loss γ_{tip} induced on μR_2 by a chromium (Cr)-coated silica-nanofiber tip (Fig. 1, B and C), which features strong absorption in the 1550-nm band. The strength of γ_{tip} was increased by enlarging the volume of the nanotip within the μR_2 mode field, resulting in a broadened resonance linewidth with no observable change in resonance frequency (Fig. 1D). A small fraction of the scattered light from the nanotip coupled back into μR_2 in the counter-

propagating (backward) direction and led to a resonance peak whose linewidth broadened as the loss increased (Fig. 1E). The resonance peak in the backward direction was $\sim 1/10^4$ of the input field, confirming that the linewidth broadening and the decrease of the resonance depth in the forward direction were due to γ_{tip} via absorption and scattering losses, but not due to back-scattering into the resonator.

In the first set of experiments, WG2 was moved away from μR_2 to eliminate the coupling between them. We investigated the evolution of the eigenfrequencies and the transmission spectra $T_{1 \rightarrow 2}$ from input port 1 to output port 2 by continuously increasing γ_{tip} while keeping κ fixed. In this configuration, losses experienced by μR_1 and μR_2 were $\gamma'_1 = \gamma_1 + \gamma_{\text{cl}}$ and $\gamma'_2 = \gamma_2 + \gamma_{\text{tip}}$, where γ_{cl} is the WG1- μR_1 coupling loss, and γ_1 and γ_2 include material absorption, scattering, and radiation losses of μR_1 and μR_2 . The coupling between the WGMRs led to the formation of two supermodes with complex eigenfrequencies $\omega_{\mp} = \omega_0 - i\chi_{\mp} \mp \beta$ whose real and imaginary parts are respectively denoted by ω'_{\mp} and ω''_{\mp} (20). Here, ω_0 is the resonance frequency of the solitary WGMRs; $\chi = (\gamma'_1 + \gamma'_2)/4$ and $\Gamma = (\gamma'_1 - \gamma'_2)/4$, respectively, quantify the total loss and the loss contrast of the WGMRs; and $\beta = \sqrt{\kappa^2 - \Gamma^2}$ reflects the transition between the strong and the weak intermode coupling regimes due to an interplay of the interresonator coupling strength κ and the loss contrast Γ (supplementary text S1). In the strong-coupling regime, quantified by $\kappa > |\Gamma|$ and real β , the supermodes had different resonance frequencies (mode splitting of 2β) but the same linewidths quantified by χ . This was reflected as two spectrally separated res-

onance modes in $T_{1 \rightarrow 2}$ [Fig. 2A (i)] and in the corresponding eigenfrequencies [Fig. 2B (i)]. Because our system satisfied $\gamma_1 + \gamma_{\text{cl}} > \gamma_2$, introducing γ_{tip} to μR_2 increased the amount of splitting until $\gamma_1 + \gamma_{\text{cl}} = \gamma_2 + \gamma_{\text{tip}}$ (that is, $\gamma'_1 = \gamma'_2$) was satisfied [Fig. 2, A (ii) and B (ii)]. Increasing γ_{tip} beyond this point gradually led to an overlap of the supermode resonances [Fig. 2A (iii)], such as to necessitate a fit to a theoretical model to extract the complex resonance parameters (supplementary text S1 and S2) (20). At $\gamma_{\text{tip}} = \gamma_{\text{tip}}^{\text{EP}}$ where $\kappa = |\Gamma|$, the supermodes coalesced at the EP. With a further increase of γ_{tip} , the system entered the weak-coupling regime, quantified by $\kappa < |\Gamma|$ and imaginary β , which led to two supermodes with the same resonance frequency but different linewidths [Fig. 2, A (iv) and B (iv)]. The resulting resonance trajectories in the complex plane clearly displayed a reversal of eigenvalue evolution (Fig. 2B): The real parts of the eigenfrequencies of the system approached each other while their imaginary parts remained equal until the EP. After passing the EP, their imaginary parts were repelled, which resulted in an increasing imaginary part for one of the eigenfrequencies and a decreasing imaginary part for the other. As a result, one of the modes became less lossy, whereas the other became more lossy (supplementary text S4).

By repeating the experiments for different κ and γ_{tip} , we obtained the eigenfrequency surfaces $\omega_{\mp}(\kappa, \gamma'_{\pm})$, whose real and imaginary parts are shown in Fig. 2, C and D. The resulting surfaces exhibit a complex square root-function topology with the special feature that a coalescence of the eigenfrequencies can be realized by varying either κ or γ_{tip} alone, which leads to a continuous thread of EPs along what may be

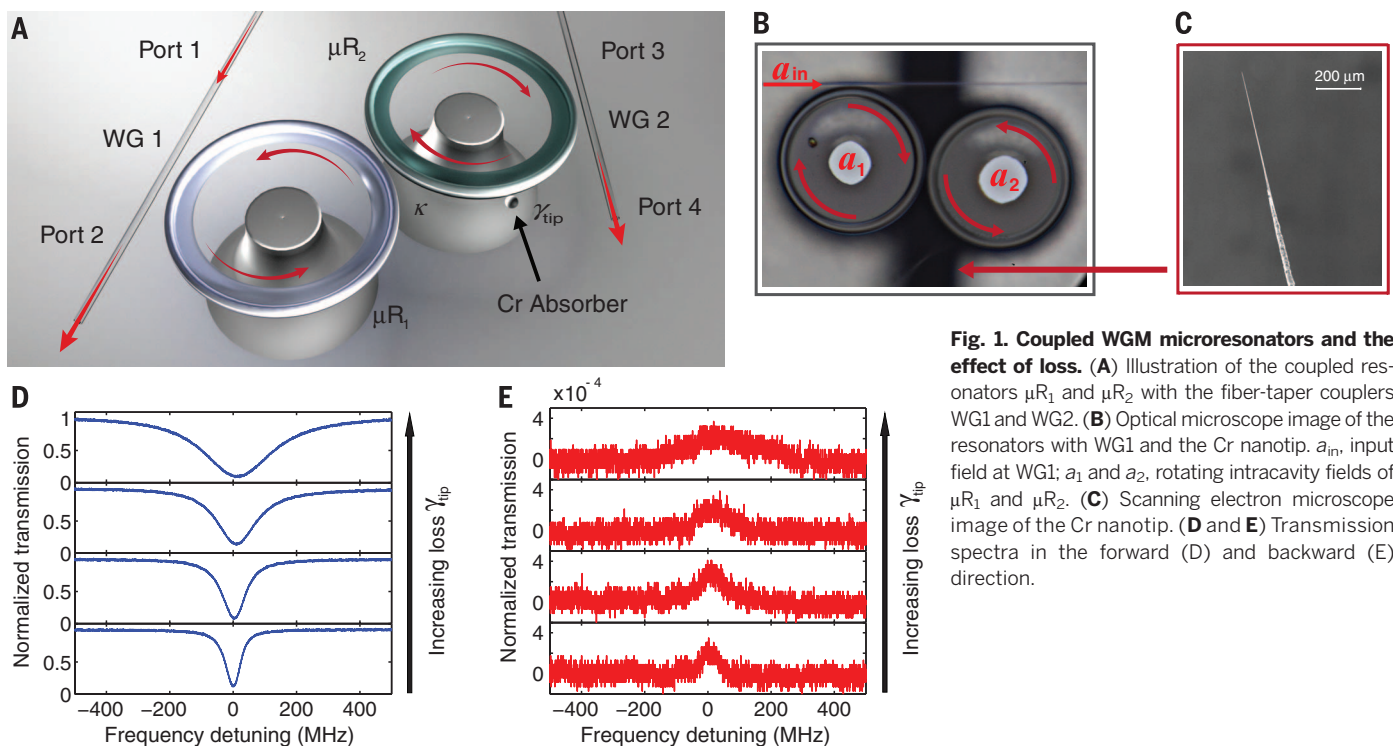


Fig. 1. Coupled WGM microresonators and the effect of loss. (A) Illustration of the coupled resonators μR_1 and μR_2 with the fiber-taper couplers WG1 and WG2. (B) Optical microscope image of the resonators with WG1 and the Cr nanotip. a_{in} , input field at WG1; a_1 and a_2 , rotating intracavity fields of μR_1 and μR_2 . (C) Scanning electron microscope image of the Cr nanotip. (D and E) Transmission spectra in the forward (D) and backward (E) direction.

called an exceptional line. As expected, the slope of this line is such that stronger κ requires higher γ_{tip} to reach the EP (supplementary text S4).

Fig. 2. Evolution of the transmission spectra and the eigenfrequencies as a function of loss γ_{tip} and interresonator coupling strength κ . (A) Transmission spectra $T_{1\rightarrow 2}$ showing the effect of loss on the supermodes. Blue and red curves denote the experimental data and the best fit using a theoretical model (supplementary text S1 and S2), respectively. (B) Evolution of the eigenfrequencies of the supermodes in the complex plane as γ_{tip} was increased. Open circles and squares are the eigenfrequencies estimated from the measured $T_{1\rightarrow 2}$. Dashed red and blue lines denote the best theoretical fit to the experimental data. (C and D) Eigenfrequency surfaces in the (κ, γ_2') parameter space (supplementary text S4).

Our second set of experiments was designed to elucidate the effect of the EP on the intracavity field intensities. For this we used both WG1 and

WG2, introducing an additional coupling loss γ_{c2} to μR_2 (that is, $\gamma_2' = \gamma_2 + \gamma_{\text{tip}} + \gamma_{c2}$). We tested two different cases by choosing different mode

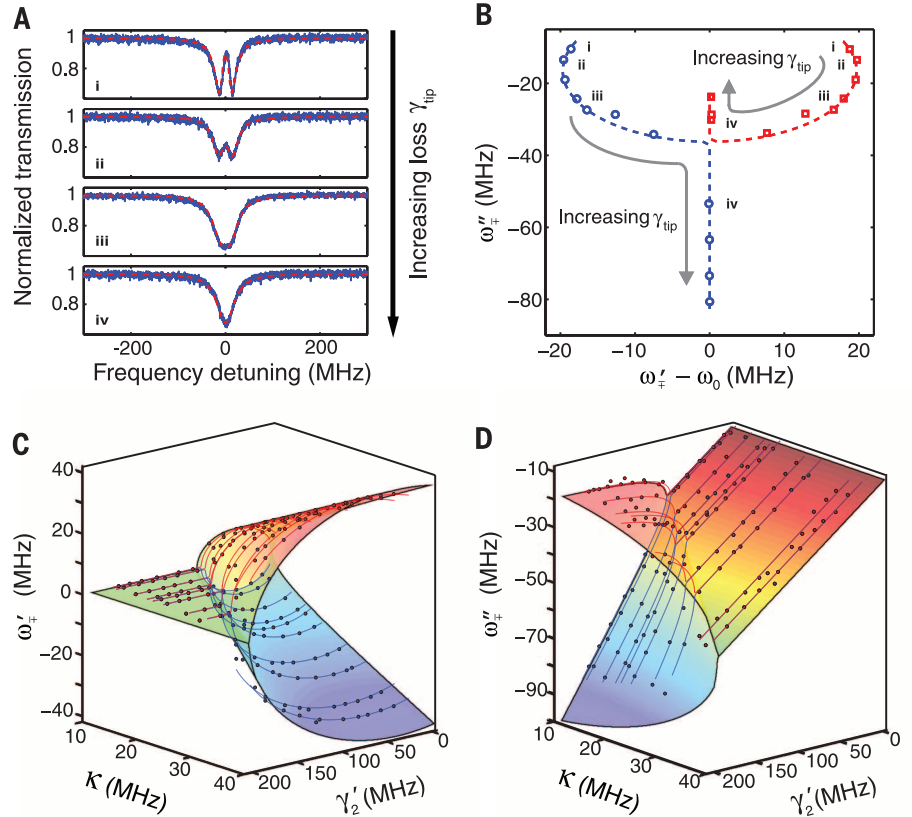
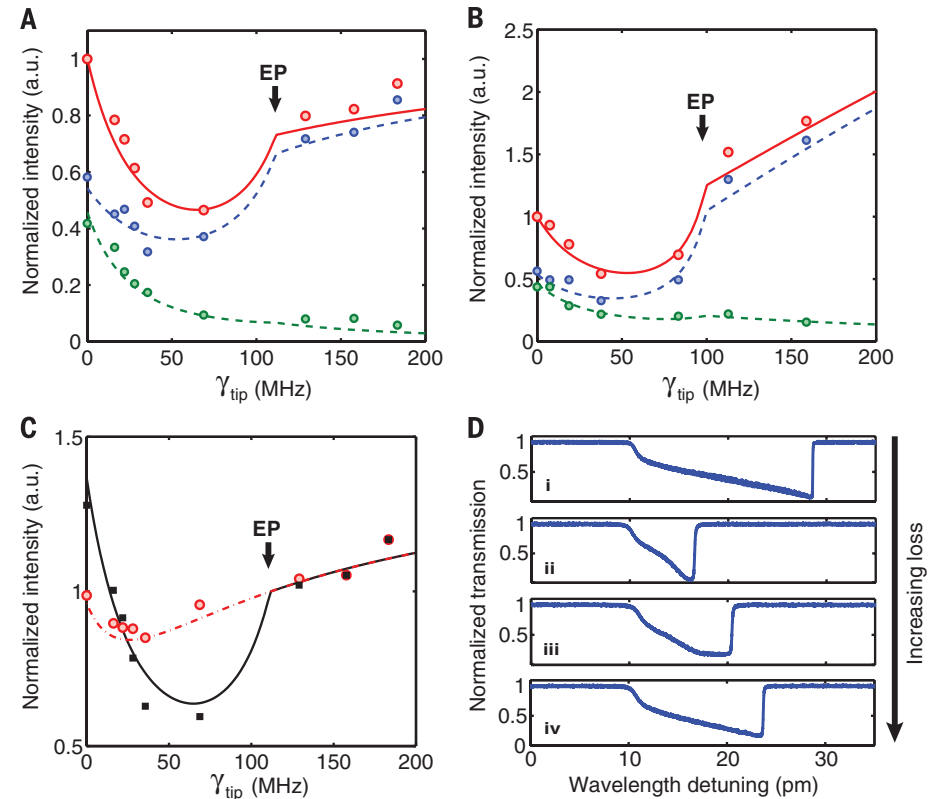


Fig. 3. Loss-induced enhancement of intracavity field intensities and thermal nonlinearity in the vicinity of an exceptional point. (A and B) Intracavity field intensities of the resonators at ω_{\mp} (blue, l_1 of μR_1 ; green, l_2 of μR_2 ; red, total l_T) for (A) case 1 and (B) case 2. Normalization was done with respect to the total intensity at $\gamma_{\text{tip}} = 0$. a.u., arbitrary units. (C) Total intracavity field intensities l_T at eigenfrequencies ω_{\mp} (black) and ω_0 (red) for case 1 (see supplementary text S5 for case 2). Normalization was done with respect to the intensity at the EP. (D) Effect of loss on nonlinear thermal response of coupled resonators (supplementary text S8): (i) solitary resonator, (ii) coupled resonators with $\gamma_{\text{tip}} = 0$, and (iii and iv) coupled resonators with increasing γ_{tip} (20). Circles in (A) to (C) and squares in (C) were calculated from experimentally obtained transmissions $T_{1\rightarrow 2}$ and $T_{1\rightarrow 4}$, whereas solid and dashed curves are from the theoretical model (supplementary text S1 to S3).



pairs in the resonators (20). In case 1, the mode in μR_1 had a higher loss than the mode in μR_2 ($\gamma_1 + \gamma_{c1} > \gamma_2 + \gamma_{c2}$); in case 2, the mode in μR_2 had a higher loss ($\gamma_1 + \gamma_{c1} < \gamma_2 + \gamma_{c2}$). The system was adjusted so that two spectrally separated supermodes were observed in the transmission spectra $T_{1 \rightarrow 2}$ and $T_{1 \rightarrow 4}$ as resonance dipped and peaked (supplementary text S3). No resonance dip or peak was observed at port 3. Using experimentally obtained $T_{1 \rightarrow 2}$ and $T_{1 \rightarrow 4}$, we estimated the intracavity fields I_1 and I_2 and the total intensity $I_T = I_1 + I_2$ as a function of γ_{tip} (Fig. 3, A to C, and supplementary text S1, S2, S5, and S6). As γ_{tip} was increased, I_T first decreased and then started to increase despite increasing loss. This loss-induced recovery of the intensity is in contrast to the expectation that the intensity would decrease with increasing loss and is a direct manifestation of the EP.

The effect of increasing γ_{tip} on I_1 and I_2 at ω_{\mp} is depicted in Fig. 3, A and B. When $\gamma_{\text{tip}} = 0$ and the system was set in the strong-coupling regime, the light input at μR_1 was freely exchanged between the resonators, establishing evenly distributed supermodes. As a result, the intracavity field intensities were almost equal. As γ_{tip} was increased, I_1 and I_2 decreased continuously at different rates until I_1 reached a minimum at $\gamma_{\text{tip}} = \gamma_{\text{tip}}^{\text{min}}$. The rate of decrease was higher for I_2 because of increasingly higher loss of μR_2 . Beyond $\gamma_{\text{tip}}^{\text{min}}$, until the EP was reached at $\gamma_{\text{tip}} = \gamma_{\text{tip}}^{\text{EP}}$, the system remained in the strong-coupling regime, but the supermode distributions were strongly affected by γ_{tip} , which led to an increase of I_1 and, hence, of I_T , whereas no appreciable change was observed for I_2 (20). Increasing γ_{tip} further pushed the system beyond the EP, thereby completing the transition from the strong-coupling to the weak-coupling regime during which I_1 increased

and kept increasing, whereas I_2 continued decreasing. This behavior is a manifestation of the progressive localization of one of the supermodes in the less lossy μR_1 and of the other supermode in the more lossy μR_2 . We conclude that the non-monotonic evolution of I_T for increasing values of γ_{tip} is the result of a transition from a symmetric to an asymmetric distribution of the supermodes in the two resonators (supplementary text S5 and S7).

The data shown in Fig. 3, A and B, also demonstrate that the initial loss contrast of the resonators affects both the amount of γ_{tip} required to bring the system to the EP and the intensity values themselves (20): Increasing γ_{tip} in case 2 increased I_T to a higher value than that at $\gamma_{\text{tip}} = 0$; in case 1, on the other hand, I_T stayed below its initial value at $\gamma_{\text{tip}} = 0$. Finally, Fig. 3C shows that the intracavity field intensities at ω_{\mp} and ω_0 coincide when $\gamma_{\text{tip}} \geq \gamma_{\text{tip}}^{\text{EP}}$; that is, after the EP transition to the weak coupling regime (20). This is a direct consequence of the coalescence of eigenfrequencies ω_{\mp} at ω_0 (supplementary text S5).

Whispering-gallery-mode microresonators (21) combine high-quality factor Q (long photon storage time, narrow linewidth) and high-finesse F (strong resonant power build-up) with microscale mode volume V (tight spatial confinement, enhanced resonant field intensity) and are thus ideal for studying quantum electrodynamics (22), optomechanics (23), lasing (24), and sensing (25–27). The ability of WGMRs to provide high intracavity field intensity and long interaction time reduces thresholds for nonlinear processes. Therefore, loss-induced reduction and the recovery of intracavity field intensities should have a direct effect on the thermal nonlinearity (28) and the Raman lasing (24, 29) in WGMRs.

Thermal nonlinearity in WGMRs is due to the temperature-dependent resonance-frequency shifts caused by material absorption of the intracavity field and the resultant heating (20, 28). In silica WGMRs, this is manifested as thermal broadening (or narrowing) of the resonance line when the wavelength of a probe laser is scanned from shorter to longer (or longer to shorter) wavelengths. In our system, thermal nonlinearity was observed in $T_{1 \rightarrow 2}$ as a shark-fin feature (Fig. 3D). With an input power of 600 μW , thermal broadening kicked in and made it impossible to resolve the individual supermodes [Fig. 3D (i and ii)]. When γ_{tip} was introduced and gradually increased, thermal nonlinearity and the associated linewidth broadening decreased at first but then gradually recovered [Fig. 3D (iii and iv)]. This aligns well with the evolution of the total intracavity field as a function of loss (supplementary text S8).

Finally, we tested the effect of the loss-induced recovery of the intracavity field intensity on Raman lasing in silica microtoroids (29, 30). The threshold for Raman lasing scales as $P_{\text{Raman-threshold}} \propto V/g_R Q^2$ (where g_R is the Raman gain coefficient), implying the importance of the pump intracavity field intensity in the process. With a pump in the 1550-nm band, Raman lasing in the silica WGMR takes place in the 1650-nm band. Figure 4 depicts the spectrum and the efficiency of Raman lasing in our system. The lasing threshold for μR_1 was $\sim 150 \mu\text{W}$ (Fig. 4B, blue curve). Keeping the pump power fixed, we introduced μR_2 , which had a much larger loss than μR_1 . This effectively increased the total loss of the system and annihilated the laser (Fig. 4A, gray curve). Introducing γ_{tip} to μR_2 helped to recover the Raman laser, whose intensity increased with increasing γ_{tip} (Fig. 4A). We also checked the lasing threshold of

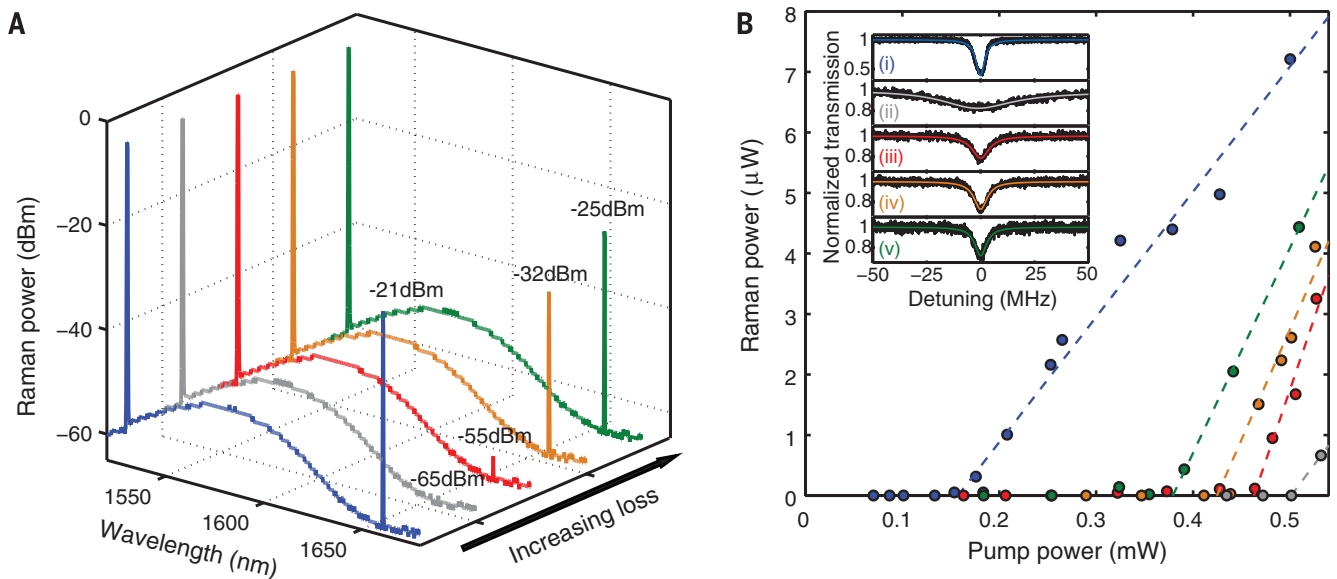


Fig. 4. Loss-induced suppression and revival of Raman lasing in silica microcavities. (A) Raman lasing spectra of coupled silica microtoroid resonators as a function of increasing loss. dBm, decibel-milliwatts. (B) Effect of loss on the threshold of Raman laser and its output power. The inset shows the normalized transmission spectra $T_{1 \rightarrow 2}$ in the pump band obtained at very weak powers $T_{1 \rightarrow 2}$ for different amounts of additional loss. Loss increases from top to bottom. The curves with the same color code in (A), (B), and the inset of (B) are obtained at the same value of additionally introduced loss.

each of the cases depicted in Fig. 4A and observed that as γ_{tip} was increased, the $P_{\text{Raman-threshold}}$ increased at first but then decreased (Fig. 4B).

These observations are in stark contrast with what one would expect in conventional systems, where the higher the loss, the higher the lasing threshold. Surprisingly, in the vicinity of an EP, less loss is detrimental and annihilates the process of interest; more loss is good because it helps to recover the process. This counterintuitive effect happens because the supermodes of the coupled system readjust themselves as loss is gradually increased. When the loss exceeds a critical value, one supermode is mostly located in the subsystem with less loss and, thus, the total field can build up more strongly (20). As our results demonstrate, this behavior also affects nonlinear processes, such as thermal broadening and Raman lasing, that rely on intracavity field intensity.

Our system provides a comprehensive platform for further studies of EPs and opens up new avenues of research on non-Hermitian systems and their behavior. Our findings may also lead to new schemes and techniques for controlling and reversing the effects of loss in other physical systems, such as in photonic crystal cavities, plasmonic structures, and metamaterials.

REFERENCES AND NOTES

- C. M. Bender, *Rep. Prog. Phys.* **70**, 947–1018 (2007).
- I. Rotter, *J. Phys. Math. Theor.* **42**, 153001 (2009).
- N. Moiseyev, *Non-Hermitian Quantum Mechanics* (Cambridge Univ. Press, Cambridge, 2011).
- W. D. Heiss, *J. Phys. A* **37**, 2455–2464 (2004).
- E. Persson, I. Rotter, H. Stockmann, M. Barth, *Phys. Rev. Lett.* **85**, 2478–2481 (2000).
- C. Dembowski et al., *Phys. Rev. Lett.* **86**, 787–790 (2001).
- S. B. Lee et al., *Phys. Rev. Lett.* **103**, 134101 (2009).
- C. M. Bender, S. Boettcher, *Phys. Rev. Lett.* **80**, 5243–5246 (1998).
- R. El-Ganainy, K. G. Makris, D. N. Christodoulides, Z. H. Musslimani, *Opt. Lett.* **32**, 2632–2634 (2007).
- C. E. Rüter et al., *Nat. Phys.* **6**, 192–195 (2010).
- A. Guo et al., *Phys. Rev. Lett.* **103**, 093902 (2009).
- A. Regensburger et al., *Nature* **488**, 167–171 (2012).
- L. Feng et al., *Nat. Mater.* **12**, 108–113 (2013).
- L. Feng et al., *Opt. Express* **22**, 1760–1767 (2014).
- H. Wenzel, U. Bandelow, H.-J. Wünsche, J. Rehberg, *IEEE J. Quantum Electron.* **32**, 69–78 (1996).
- M. V. Berry, *J. Mod. Opt.* **50**, 63–81 (2003).
- M. Liertzer et al., *Phys. Rev. Lett.* **108**, 173901 (2012).
- B. Peng et al., *Nat. Phys.* **10**, 394–398 (2014).
- M. Brandstetter et al., *Nat. Commun.* **5**, 4034 (2014).
- Supplementary materials are available on Science Online.
- K. J. Vahala, *Nature* **424**, 839–846 (2003).
- D. O'Shea, C. Junge, J. Volz, A. Rauschenbeutel, *Phys. Rev. Lett.* **111**, 193601 (2013).
- T. J. Kippenberg, K. J. Vahala, *Science* **321**, 1172–1176 (2008).
- L. He, S. K. Ozdemir, L. Yang, *Laser & Photon. Rev.* **7**, 60–82 (2013).
- X. Fan et al., *Anal. Chim. Acta* **620**, 8–26 (2008).
- F. Vollmer, S. Arnold, *Nat. Methods* **5**, 591–596 (2008).
- Z. Zhu et al., *Nat. Photonics* **4**, 46–49 (2010).
- T. Carmon, L. Yang, K. Vahala, *Opt. Express* **12**, 4742–4750 (2004).
- S. M. Spillane, T. J. Kippenberg, K. J. Vahala, *Nature* **415**, 621–623 (2002).
- S. K. Ozdemir et al., *Proc. Natl. Acad. Sci. U.S.A.* **111**, E3836–E3844 (2014).

ACKNOWLEDGMENTS

Ş.K.O. and L.Y. conceived the idea and designed the experiments. B.P. and Ş.K.O. performed the experiments with help from H.Y. and F.M. Theoretical background and simulations were provided by B.P., Ş.K.O., S.R., M.L., C.M.B., and F.N. All authors discussed the results, and Ş.K.O., S.R., and L.Y. wrote the manuscript with input from all authors. This work was supported by Army Research

Office (ARO) grant no. W911NF-12-1-0026. C.M.B. was supported by U.S. Department of Energy grant no. DE-FG02-91ER40628. F.N. is partially supported by the RIKEN iTHES Project, Multidisciplinary University Research Initiatives (MURI) Center for Dynamic Magneto-Optics, Grant-in-Aid for Scientific Research (S). S.R. and M.L. are supported by the Vienna Science and Technology Fund (WWTF) project no. MA09-030 and by the Austrian Science Fund (FWF) project no. SFB-IR-ON F25-P14, SFB/NextLite F49-P10.

SUPPLEMENTARY MATERIALS

www.sciencemag.org/content/346/6207/328/suppl/DC1
Supplementary Text
Figs. S1 to S16
Table S1
References (31–34)

27 June 2014; accepted 11 September 2014
10.1126/science.1258004

QUANTUM ELECTRONICS

Cavity quantum electrodynamics with many-body states of a two-dimensional electron gas

Stephan Smolka,^{1,*} Wolf Wuester,^{1,2,*} Florian Haupt,¹ Stefan Faelt,^{1,2} Werner Wegscheider,² Ataç Imamoglu^{1†}

Light-matter interaction has played a central role in understanding as well as engineering new states of matter. Reversible coupling of excitons and photons enabled groundbreaking results in condensation and superfluidity of nonequilibrium quasiparticles with a photonic component. We investigated such cavity-polaritons in the presence of a high-mobility two-dimensional electron gas, exhibiting strongly correlated phases. When the cavity was on resonance with the Fermi level, we observed previously unknown many-body physics associated with a dynamical hole-scattering potential. In finite magnetic fields, polaritons show distinct signatures of integer and fractional quantum Hall ground states. Our results lay the groundwork for probing nonequilibrium dynamics of quantum Hall states and exploiting the electron density dependence of polariton splitting so as to obtain ultrastrong optical nonlinearities.

Strong electric-dipole coupling of excitons in an intrinsic semiconductor quantum well (QW) to microcavity photons leads to the formation of mixed light-matter quasiparticles called cavity-polaritons (1, 2). In contrast to excitons, optical excitations from a two-dimensional electron gas (2DEG) show many-body effects associated with the abrupt turn-on of a valence-band hole-scattering potential. The resulting absorption spectrum exhibits a power-law divergence, stemming from final-state interaction effects that lead to orthogonal initial and final many-body wave functions, and is referred to as Fermi-edge singularity (3). Despite initial attempts (4–6), the nature of strong coupling of a Fermi-edge singularity, rather than an exciton, to a microcavity mode remained largely unexplored.

We investigated a 2DEG in a modulation-doped GaAs QW embedded in a distributed Bragg reflector (DBR) microcavity (Fig. 1A). We used this system to analyze two distinct problems: In the absence of an external magnetic field ($B_z = 0$), optical excitations from a 2DEG are simultaneously subject to Coulomb interactions and strong cavity coupling, which lead

to the formation of Fermi-edge polaritons—a many-body excitation with a dynamical valence-hole scattering potential (7). In the $B_z \neq 0$ limit, we establish cavity quantum electrodynamics (QED) as a new paradigm for investigating integer and fractional quantum Hall (QH) states (8) in which information about a strongly correlated electronic ground state is transcribed onto the reflection and transmission amplitudes of a single-cavity photon.

The dispersion of the relevant electronic states when $B_z = 0$ is shown in Fig. 1B, left. The Fermi energy E_F is tuned by applying a gate voltage (V_g) between a p-doped GaAs top layer and the 2DEG. When $B_z \neq 0$, the electronic states form discrete Landau levels (LLs) (Fig. 1B, right). Each (spin-resolved) LL has a degeneracy $e B_z/h$; the filling factor $\nu = n_e h/(e B_z)$ determines the number of filled LLs at a given electron density n_e . We studied two different samples with gate-tunable n_e : sample A exhibits an electron mobility of $\mu = 2 \times 10^5 \text{ cm}^2(\text{V s})^{-1}$ at $n_e = 1.0 \times 10^{11} \text{ cm}^{-2}$ (9). Sample B exhibits an order-of-magnitude-higher mobility of $\mu = 2.5 \times 10^6 \text{ cm}^2(\text{V s})^{-1}$ at $n_e = 2.3 \times 10^{11} \text{ cm}^{-2}$.

The differential reflectivity (dR) (9) spectra of sample A (blue) is shown in Fig. 1D as the electron density n_e in the 2DEG is varied from $n_e < 2 \times 10^{10} \text{ cm}^{-2}$ to $n_e = 8 \times 10^{10} \text{ cm}^{-2}$. The cavity mode is visible as a dR peak at 1521 meV. Changing n_e modifies the nature of elementary optical excitations: At low electron densities

¹Institute of Quantum Electronics, Eidgenössische Technische Hochschule (ETH) Zurich, 8093 Zurich, Switzerland. ²Solid State Physics Laboratory, ETH Zurich, 8093 Zurich, Switzerland.

*These authors contributed equally to this work. †Corresponding author. E-mail: imamoglu@phys.ethz.ch